Princeton Plasma Physics Laboratory

PPPL-4142

PPPL-4142

Gyrokinetic Simulation of Global Turbulent Transport Properties in Tokamak Experiments

W.X. Wang, Z. Lin, W.M. Tang, W.W. Lee, S. Ethier,
J.L.V. Lewandowski, G. Rewoldt, T.S. Hahm, and J. Manickam

January 2006

Prepared for the U.S. Department of Energy under Contract DE-AC02-76CH03073.

Princeton Plasma Physics Laboratory
Report Disclaimers

Full Legal Disclaimer

Trademark Disclaimer

PPPL Report Availability

Princeton Plasma Physics Laboratory

This report is posted on the U.S. Department of Energy's Princeton Plasma Physics Laboratory Publications and Reports web site in Fiscal Year 2006.

The home page for PPPL Reports and Publications is:

http://www.pppl.gov/pub_report/

Office of Scientific and Technical Information (OSTI):

Available electronically at: http://www.osti.gov/bridge.

Available for a processing fee to U.S. Department of Energy and its contractors, in paper from:

U.S. Department of Energy
Office of Scientific and Technical Information
P.O. Box 62
Oak Ridge, TN 37831-0062

Telephone: (865) 576-8401

Fax: (865) 576-5728

E-mail: reports@adonis.osti.gov

Gyrokinetic Simulation of Global Turbulent Transport Properties in Tokamak Experiments

W. X. Wang, Z. Lin[1], W. M. Tang, W. W. Lee, S. Ethier,

J. L. V. Lewandowski, G. Rewoldt, T. S. Hahm, J. Manickam

Plasma Physics Laboratory, Princeton University

P. O. Box 451, Princeton, New Jersey 08543

[1]Department of Physics and Astronomy, University of California, Irvine, California 92697

January 20, 2006

Abstract

A general geometry gyrokinetic model for particle simulation of plasma turbulence in tokamak experiments is described. It incorporates the comprehensive influence of non-circular cross section, realistic plasma profiles, plasma rotation, neoclassical (equilibrium) electric fields, and Coulomb collisions. An interesting result of global turbulence development in a shaped tokamak plasma is presented with regard to nonlinear turbulence spreading into the linearly stable region. The mutual interaction between turbulence and zonal flows in collisionless plasmas is studied with a focus on identifying possible nonlinear saturation mechanisms for zonal flows. A bursting temporal behavior with a period longer than the geodesic acoustic oscillation period is observed even in a collisionless system. Our simulation results suggest that the zonal flows can drive turbulence. However, this process is too weak to be an effective zonal flow saturation mechanism.

PACS numbers: 52.35.Ra, 52.65.Tt, 52.65.Rr, 52.55.Fa

I. INTRODUCTION

Understanding turbulence and associated transport in toroidal plasmas[1–3] is one of the key issues in magnetic fusion research. In the past decade as computer resources rapidly increased and advanced numerical algorithms were developed, significant progress was made for this long-standing complicated issue through computer simulation based on various approaches.[4–15] Among them the first-principles based gyrokinetic particle approach[16] has been widely employed. The simulation study carried out by the gyrokinetic toroidal code GTC[8] represents one of the most productive examples. GTC was originally developed to focus on fundamental nonlinear turbulence physics. It is a full-torus global code using a global field-line-following mesh and a real space field solver. Global turbulence simulations for toroidal plasmas are highly demanding for the following reasons: (i) the turbulence-generated zonal flow contains radial scales as large as the system size, even though the turbulence itself is on the much smaller scale of the gyroradius; (ii) the equilibrium $\mathbf{E} \times \mathbf{B}$ shear flow, which also plays an important role in determining turbulence levels, typically has the large scale size of the plasma minor radius; (iii) turbulence spreading to the linearly stable zone results in nonlocal transport, which is a truly global phenomenon. To pose the simplest problem while keeping the important global physics properties, a simplified model was utilized in the previous simulations, such as simple magnetic geometry with a large aspect ratio circular concentric cross section and neglect of the effect of radial variation of pressure. This proved to be an effective means of gaining key insights into the complexity of the toroidal turbulence system. As a result, the previous simulation studies have led to a number of important understandings with regard to zonal flow effects, transport scalings with collisionality and device size, turbulence spreading, etc.[8,17–19] While such a simplified model is a useful tool to separate and clarify fundamental physics issues, more realistic features are needed as the research moves forward. Particularly for simulating turbulence phenomena in tokamak experiments, a more comprehensive model is needed which consistently incorporates the influence of general geometry, realistic plasma profiles, plasma flow, neoclassical equilibrium, Coulomb collisions and other features. In this paper we present such a model with emphasis on the general geometry capability, which has now been implemented based on GTC architecture. The developed

general geometry simulation is interfaced with TRANSP, a widely used experimental data analysis software tool for specifying experimental plasma profiles of temperature, density and toroidal angular velocity, and also with various numerical MHD equilibrium codes, including the JSOLVER, QSOLVER and ESC codes.

Global turbulence fluctuation levels and associated transport are determined by both local and nonlocal physics. Turbulence propagation in the radial direction results in transport nonlocality which should be addressed by global simulation. The new capability is applied to shaped plasmas with DIII-D geometry to examine the ion temperature gradient (ITG) turbulence spreading phenomena and the global turbulence evolution process. We also investigate the nonlinear interplay between turbulence and zonal flow, which is essentially a local process. As an attempt to understand the nonlinear zonal flow dissipation, which is needed to saturate zonal flow and to explain the mutual self-regulation observed in collisionless simulations, we study the process of zonal flow driving turbulence. Our simulation results suggest that the coupling of zonal flows to turbulence and associated energy transfers are much weaker, compared to the opposite process in ITG turbulence.

The rest of the paper is organized as follows. The general geometry simulation model is described in Sec. II. We describe the coordinate system and mesh construction, with the consideration of shaped equilibrium geometry and strong nonuniformity of the global temperature profile; we detail the calculation of the gyrokinetic transformation of fluctuations between particle position and guiding center position in generalized geometry; the system of basic gyrokinetic equations used in this generalized simulation model is also presented. Our simulation results is presented in Sec. III. These include linear and nonlinear ITG benchmarks in a simple geometry, global turbulence evolution in a DIII-D-shaped plasma, and turbulence self-regulation in collisionless plasma. Concluding remarks are summarized in Sec. IV.

II. GENERAL GEOMETRY GYROKINETIC PARTICLE SIMULATION MODEL

A. Coordinate system and mesh construction

Magnetic flux coordinates, in which the radial coordinate labels magnetic surfaces, are generally used for toroidal systems and associated with MHD equilibria. Our gyrokinetic simulation in principle can use arbitrary flux coordinates with straight field lines. In the flux coordinates, the global field-line-following mesh, which possesses the highest efficiency by capturing the flute-type character of the drift wave turbulence in toroidal plasmas, can be easily constructed. A preferable flux coordinate can be chosen in terms of different requirements. A symmetric coordinate system in which the toroidal angle φ is chosen to be the azimuthal angle of cylindrical coordinates is preferable in many cases. These coordinates are relatively uniform compared to others which have been previously used, and advantageous for constructing a relatively regular mesh in real space for strongly shaped plasmas. It also facilitates straightforward visualization with the poloidal plane defined with the physical angle φ. The radial coordinate is defined as $r = \sqrt{\psi/\psi_e}$ where ψ and ψ_e are the toroidal flux and its value on the plasma boundary, respectively. This same radial coordinate is widely used in the experimental community.

Because of the flute-type character of drift wave turbulence in toroidal plasmas, with $k_{\|} \ll k_{\perp}$, where $k_{\|}$ and $k_{\perp}$ are the parallel and perpendicular wave numbers, respectively, GTC uses a field-line-following mesh which shows high efficiency for calculating the turbulent field. For drift wave turbulence, the spatial scale length in the perpendicular direction is generally in correlation with the local gyroradius $\rho_j \propto \sqrt{T_j}$, which may vary substantially from the core to the edge of the plasma. For instance, it is common in National Spherical Torus Experiment (NSTX) plasmas that the ion temperature changes from $\sim keV$ in the core to $\sim 10eV$ near the separatrix region at the plasma edge. Therefore, for a global simulation, which includes the entire radial domain, it is important to use a nonuniform grid with the grid size in the perpendicular direction correlated with the local gyroradius for improved spatial resolution and efficiency. To this end, we re-scale the radial coordinate by defining ρ

as follows:

$$\frac{d\rho}{dr} = \sqrt{T_c/T_i(r)}, \tag{1}$$

where T_c is the temperature at a reference radial location. Working with the new coordinate ρ, we use an evenly spaced radial grid, which offers great convenience for frequent operations such as particle sorting, charge deposition, gathering, etc. This allows the grid size in real space to be correlated with the local gyroradius: $\Delta r \sim \sqrt{T_i(r)/T_c}$. In the poloidal direction, the grid size $\Delta\theta(r)$ is uniform on a flux surface, while varying over different flux surfaces. The grid size $\Delta\theta(r)$ is determined so as to make the poloidal arc length Δl_θ near the mid-plane correlated with ρ_i. An example of such a grid on the toroidal plane $\varphi = 0$ is shown in Fig.1. Generally, a two-dimensional mesh on the $\varphi = 0$ plane is set up first. A three-dimensional mesh is constructed by following each (approximate) field line, which starts at a grid point on the $\varphi = 0$ plane and has $\bar{q}(r)\theta - \varphi$ =constant, with $\bar{q}$ slightly changed from the usual safety factor $q(r)$ so that the approximate field lines will lead back to one of the grid points on the $\varphi = 0$ plane. Two methods for enforcing toroidal periodicity have been implemented. One method is to map the grid at $\zeta = 0$ to the grid at $\zeta = 2\pi$ using interpolation, which results in some spatial damping. Another method is to allow the grid to slightly depart from the magnetic field lines in order to match the grid points, which requires a chain rule in calculating the parallel derivatives. With either approach, there is no approximation in the representation of the toroidal geometry.

The gyrokinetic particles are followed in general flux coordinates using guiding center Lagrangian equations, instead of Hamiltonian equations that require construction of canonical variables[22] which are complicated forms in general geometry and inconvenient to use. The guiding center Lagrangian obtained by Littlejohn has the following normalized form[22,23]

$$L(\mathbf{x}, \dot{\mathbf{x}}; t) = (\mathbf{A} + \rho_{\|}\mathbf{B}) \cdot \mathbf{v} - H, \tag{2}$$

with the guiding center Hamiltonian $H = \rho_{\|}^2 B^2/2 + \mu B + \Phi$. Here, the magnetic field $\mathbf{B} = \nabla \times \mathbf{A}$, $\rho_{\|} = v_{\|}/B$ is the parallel gyroradius, μ is the magnetic moment, and Φ is the electric potential. The independent variables are $\mathbf{x} = (r, \theta, \varphi, \rho_{\|})$. The particle guiding drift motion

is governed by the Lagrangian equations

$$\frac{d}{dt}\left(\frac{\partial}{\partial \dot{x}_i}L\right) - \frac{\partial}{\partial x_i}L = 0. \tag{3}$$

The obtained equations for $d\mathbf{x}/dt$ are suitable for any generalized flux coordinates.

B. Gyrokinetic transformation

One of the important elements of the gyrokinetic formalism[16,24–28] is concerned with the transformation of fluctuations between the particle position $\vec{x}$ and the guiding center position $\vec{R}$. The fluctuations, such as the potential ϕ and the ion density δn_i in the two coordinates are connected by the gyrokinetic transformation which is expressed as follows

$$\bar{\phi}(\vec{R},\mu) = \frac{1}{2\pi}\int \phi(\vec{x})\delta(\vec{x}-\vec{R}-\vec{\rho})d\vec{x}d\Theta, \tag{4}$$

$$\tilde{\phi}(\vec{x}) = \frac{1}{2\pi}\int \bar{\phi}(\vec{R},\mu)f_{Mi}(\vec{R},\mu,v_{\|})\delta(\vec{R}-\vec{x}+\vec{\rho})d\vec{R}d\mu dv_{\|}d\Theta, \tag{5}$$

$$\bar{\delta n_i}(\vec{x}) = \frac{1}{2\pi}\int \delta f_i(\vec{R},\mu,v_{\|})\delta(\vec{R}-\vec{x}+\vec{\rho})d\vec{R}d\mu dv_{\|}d\Theta, \tag{6}$$

where $\vec{\rho}$ is the gyroradius vector, Θ is the gyrophase, f_{Mi} is assumed to be Maxwellian and δf_i is the perturbed ion distribution function. In a gyrokinetic simulation, the quantities are is calculated either in real space or in Fourier space. In real space the transformation is carried out by the four-point averaging scheme.[29] The exact gyro-average is performed on a gyro-plane perpendicular to the magnetic field with 4 points evenly spaced on a gyro-orbit. Because the grid points on which fluctuations ϕ and δn_i are calculated are set up on poloidal planes, it is much more convenient to perform the gyro-average on poloidal planes instead of on gyro-planes. In the case of the simple geometry of large aspect ratio circular concentric cross section, the difference between a poloidal plane and a gyro-plane is neglected in doing the gyro-average. An accurate treatment for the gyro-average in general geometry is obtained by taking into account the finite ratio of the poloidal to the total magnetic field B_p/B, which separates the poloidal plane from the gyro-plane. By projection to the poloidal plane, a gyro-orbit becomes an elliptic orbit (Fig.2). In the direction of $(\nabla\varphi \times \mathbf{B}) \times \nabla\varphi$, the gyroradius is elongated by a factor of $1/\cos\alpha$ while there is no change in the $\nabla\varphi \times \mathbf{B}$

direction. Here, $\cos\alpha = \mathbf{B}\cdot\nabla\varphi/B|\nabla\varphi| = \psi'/\mathcal{J}B|\nabla\varphi|$, with $\psi' \equiv d\psi/dr$ and the Jacobian $\mathcal{J} = (\nabla r\times\nabla\theta\cdot\nabla\varphi)^{-1} > 0$ (right handed). The four points used for the gyro-average are chosen to be located on the axes $(\nabla\varphi\times\mathbf{B})\times\nabla\varphi$ and $\nabla\varphi\times\mathbf{B}$. An ion spends approximately the same amount of time on each quarter of the ellipse. To locate the positions of the four points relative to the guiding center, we first calculate the directional derivatives in the two directions which are defined as $dA/dl \equiv \hat{\mathbf{l}}\cdot\nabla A$ for any function A, where $\hat{\mathbf{l}}$ is unit vector in direction $\mathbf{l}$. In the $\nabla\varphi\times\mathbf{B}$ direction

$$\frac{dr}{dl_1} = \frac{[(g^{r\varphi})^2 - g^{\varphi\varphi}g^{rr}]/q + g^{rr}g^{\theta\varphi} - g^{r\varphi}g^{r\theta}}{\sqrt{g^{\varphi\varphi}B^2/\psi'^2 - 1/\mathcal{J}^2}}, \tag{7}$$

$$\frac{d\theta}{dl_1} = \frac{[g^{\varphi\theta}g^{r\varphi} - g^{\varphi\varphi}g^{\theta\varphi}]/q + g^{r\theta}g^{\theta\varphi} - g^{r\varphi}g^{\theta\theta}}{\sqrt{g^{\varphi\varphi}B^2/\psi'^2 - 1/\mathcal{J}^2}}; \tag{8}$$

in the $(\nabla\zeta\times\vec{B})\times\nabla\zeta$ direction

$$\frac{dr}{dl_2} = -\frac{g^{r\varphi}}{\mathcal{J}\sqrt{g^{\varphi\varphi}}\sqrt{g^{\varphi\varphi}B^2/\psi'^2 - 1/\mathcal{J}^2}}, \tag{9}$$

$$\frac{d\theta}{dl_2} = \frac{g^{\varphi\varphi}/q - g^{\theta\varphi}}{\mathcal{J}\sqrt{g^{\varphi\varphi}}\sqrt{g^{\varphi\varphi}B^2/\psi'^2 - 1/\mathcal{J}^2}}, \tag{10}$$

where the metric tensor $g^{\alpha\beta} = \nabla\alpha\cdot\nabla\beta$. The four points used for the ion gyro-average are determined by

$$r_j = r_0 + \Delta r_j, \quad \theta_j = \theta_0 + \Delta\theta_j, \quad \varphi_j = \varphi_0, \quad j = 1,2,3,4 \tag{11}$$

with

$$\Delta r_{1,2} = \pm\frac{dr}{dl_1}\rho_i, \quad \Delta\theta_{1,2} = \pm\frac{d\theta}{dl_1}\rho_i, \quad \Delta r_{3,4} = \pm\frac{dr}{dl_2}\frac{\rho_i}{\cos\alpha}, \quad \Delta\theta_{3,4} = \pm\frac{d\theta}{dl_2}\frac{\rho_i}{\cos\alpha}. \tag{12}$$

The calculation of the potential $\tilde{\phi}(\vec{x})$ in terms of $\phi(\vec{x})$ involves the double averaging process.[30] Following the above method we can extend the previous calculation of $\tilde{\phi}(\vec{x})$ in Ref. 30 to general geometry, taking into account finite B_θ/B. The double average is made along the elliptic orbit projected on the poloidal plane as shown in Fig.3 where $\tilde{\phi}$ at the center point is the four-point averages of $\bar{\phi}$ on the X points, which are other four-point average of

ϕ on the O points. The average over the distribution function is accomplished by carefully sampling different gyroradii.[30]

It is noted that the four-point averaging scheme is accurate for $k_\perp \rho_i \leq 2$ modes. To resolve shorter wavelength modes, we may use more points for the averaging process. An implicit assumption of the 4-point averaging scheme described above is that the equilibrium scale lengths L_p and L_B of the pressure and magnetic field are much larger than the ion gyroradius, which is consistent with the gyrokinetic ordering.

C. Basic equations

The gyrokinetic particle distribution is expressed as $f = f_0 + \delta f$. Here we separate the turbulence perturbation δf from the equilibrium distribution f_0. In the electrostatic limit the ion gyrokinetic equation for δf_i with μ and $v_\parallel$ as independent velocity variables is

$$\frac{\partial \delta f_i}{\partial t} + (v_\parallel \hat{b} + \vec{v_{E_0}} + \vec{v_E} + \vec{v_d}) \cdot \nabla \delta f_i - \hat{b^*} \cdot \nabla (\mu B + \frac{e}{m_i}\Phi_0 + \frac{e}{m_i}\bar{\phi}) \frac{\partial \delta f_i}{\partial v_\parallel}$$

$$= -\vec{v_E} \cdot \nabla f_0 + \hat{b^*} \cdot \nabla (\frac{e}{m_i}\bar{\phi}) \frac{\partial f_0}{\partial v_\parallel} + C_i^l(\delta f_i). \tag{13}$$

Here $\vec{v_{E_0}}$ and $\vec{v_E}$ are the $\mathbf{E}\times\mathbf{B}$ drift velocities corresponding to the equilibrium potential Φ_0 and the fluctuation potential $\bar{\phi}$ respectively, $\vec{v_d}$ is the ∇B drift velocity, $\hat{\mathbf{b}}^* = \hat{\mathbf{b}} + \rho_\parallel \hat{\mathbf{b}} \times (\hat{\mathbf{b}} \cdot \nabla \hat{\mathbf{b}})$ with $\hat{\mathbf{b}} = \mathbf{B}/B$, and C_i^l is the linearized Coulomb collision operator. Note that a parallel velocity nonlinearity term which is one order higher[24] is retained in the equation. This term is required in order to maintain energy conservation.[25,26] The equilibrium distribution function f_0 is determined by the neoclassical dynamics and obeys

$$\frac{\partial f_0}{\partial t} + (v_\parallel \hat{b} + \vec{v_{E_0}} + \vec{v_d}) \cdot \nabla f_0 - \hat{b^*} \cdot \nabla (\mu B + \frac{e}{m_i}\Phi_0) \frac{\partial f_0}{\partial v_\parallel} = C_i(f_0, f_0). \tag{14}$$

The lowest order solution of Eq.14 is a shifted Maxwellian consistent with plasma rotation:

$$f_0 = f_{SM} = n(r,\theta)(\frac{m_i}{2\pi T_i})^{3/2} e^{-\frac{m_i}{T_i}[\frac{1}{2}(v_\parallel - U_i)^2 + \mu B]}, \tag{15}$$

where the parallel flow velocity U_i is associated with the toroidal rotation by $U_i = I\omega_t/B$ with ω_t the toroidal angular velocity and I the toroidal current, and $n(r,\theta)$ is the ion density

$n(r,\theta) = N(r)e^{\frac{m_i U_i^2}{2T_i} - \frac{e\tilde{\Phi}_0}{T_i}}$. The total equilibrium potential consists of two parts $\Phi_0 = \langle\Phi_0\rangle + \tilde{\Phi}_0$. Here, $\langle\rangle$ denotes a flux surface average. The poloidally varying component $\tilde{\Phi}_0$ can be generated by the centrifugal force which drives a charge separation on a magnetic surface in strongly rotating plasmas.[31] Generally the radial potential $\langle\Phi_0\rangle$ is dominant. The equilibrium radial electric field can be calculated from a first-principles based particle simulation of neoclassical dynamics with important finite orbit effects,[32,33] or obtained by direct experimental measurement if available. For equilibrium toroidal plasmas, a shifted Maxwellian with either model or experimental profiles $\langle n(r,\theta)\rangle$, $T_i(r)$ and $\omega_t(r)$ are prescribed for the ions. The electron dynamics is described by the drift kinetic equation, neglecting the finite gyroradius effect. The electron guiding center distribution is represented as $f_e = f_{e0} - (e\delta\phi/T_e)f_{e0} + \delta h_e$, with turbulence potential $\delta\phi = \phi - \langle\phi\rangle$. The equilibrium distribution f_{e0} satisfies the electron version of Eq. 14 and can be approximated by a shifted Maxwellian containing a parallel flow, similar to that for the ions. The second term represents the adiabatic electron response to the potential fluctuation due to the fast electron motion. The nonadiabatic electron distribution δh_e is determined by

$$\frac{\partial \delta h_e}{\partial t} + (v_\parallel \hat{b} + v_{E_0}^{\vec{}} + v_E^{\vec{}} + v_d^{\vec{}}) \cdot \nabla \delta h_e - \hat{b^*} \cdot \nabla(\mu B + \frac{e}{m_e}\Phi_0 + \frac{e}{m_e}\phi)\frac{\partial \delta h_e}{\partial v_\parallel}$$

$$= -v_E^{\vec{}} \cdot \nabla f_{e0} + \hat{b^*} \cdot \nabla(\frac{e}{m_e}\phi)\frac{\partial f_{e0}}{\partial v_\parallel} + \frac{e}{T_e}\frac{\partial \delta\phi}{\partial t} f_{e0} + (v_\parallel \hat{b} + v_{E_0}^{\vec{}} + v_E^{\vec{}} + v_d^{\vec{}}) \cdot \nabla \left(\frac{e\delta\phi}{T_e}\right) f_{e0} + C_e^l(\delta h_e). \quad (16)$$

Again, the parallel velocity nonlinearity is retained here for δh_e. At present the trapped electron dynamics described by Eq. 16 is treated as a higher order correction to the adiabatic response via a hybrid model[34,35] in the electrostatic limit. To include full electron dynamics, we will use the split-weight scheme[36,37] to solve Eq. 16.

The electrostatic fluctuation potential is divided into a turbulence part plus a zonal flow part: $\phi = \delta\phi + \phi_{00}$ with $\phi_{00} \equiv \langle\phi\rangle$. This expression emphasises the critical role of turbulence-generated zonal flow in determining the turbulence and the associated transport level. For the turbulence potential, the gyrokinetic Poisson equation[16] becomes

$$\left(1 + \frac{T_i}{T_e}\right)\frac{e\delta\phi}{T_i} - \frac{e\widetilde{\delta\phi}}{T_i} = \frac{\delta\bar{n}_i - \langle\delta\bar{n}_i\rangle}{n_0} - \frac{\delta n_e^{(1)} - \langle\delta n_e^{(1)}\rangle}{n_0}, \quad (17)$$

where $\delta\bar{n}_i = \int d^3v \delta f_i$ is the ion fluctuation density of guiding centers and $\delta n_e^{(1)} = \int d^3v \delta h_e$ is the nonadiabatic density of electrons. Because the zonal flow has a larger spatial scale than the turbulence fluctuations, it is advantageous to solve for it separately in our simulations. The generalized equation for zonal flow in shaped geometry is obtained as:

$$\frac{1}{\mathcal{V}_r'}\frac{d}{dr}\left[\frac{d\phi_{00}}{dr}\mathcal{V}_r'\langle g^{rr}\rangle\right] = \frac{1}{\mathcal{V}_r'}\frac{d}{dr}\left\{\frac{d}{dr}\left[\frac{T_i}{e}(\frac{\langle\delta\bar{n}_i\rangle}{n_0} - \frac{\langle\delta n_e^{(1)}\rangle}{n_0})\right]\mathcal{V}_r'\langle g^{rr}\rangle\right\} - \langle\frac{1}{\rho_i^2}\rangle\frac{T_i}{e}\left(\frac{\langle\delta\bar{n}_i\rangle}{n_0} - \frac{\langle\delta n_e^{(1)}\rangle}{n_0}\right), \tag{18}$$

where $\mathcal{V}_r' = \oint d\theta d\varphi \mathcal{J}$. In Eq. 18 we use the Pade approximation $\Gamma_0(b) \equiv I_0(b)e^{-b} \approx 1/(1+b)$ with I_0 the modified Bessel function and $b = (k_\perp\rho_i)^2$, and $\left\langle\tilde{\phi}\right\rangle \approx \widetilde{\langle\phi\rangle}$. The later approximation is not well justified for low aspect ratio geometry. A generalized field solver such as in Ref. 38 may help to remove this approximation.

III. SIMULATION RESULTS

The general geometry model has been implemented based on GTC architecture. In this section we present simulation results, including linear and nonlinear benchmarks, nonlocal ITG instability, nonlinear turbulence spreading in a shaped plasma, and turbulence self-regulation in a collisionless plasma.

A. Benchmarks

The general geometry model and simulation has been benchmarked, in the large aspect ratio circular concentric geometry limit, against the original GTC code, which uses a simple analytical MHD equilibrium. For this benchmark, a corresponding numerical equilibrium is produced for the general geometry GTC. The numerical equilibrium includes a small Shafranov shift due to non-zero plasma beta and higher order (in the small inverse aspect ratio) corrections, which are neglected in the analytical equilibrium. The benchmarks are carried out for ion temperature gradient modes with a simplified adiabatic response for the electron dynamics. The representative parameters for the familiar Cyclone case[10] are used here: inverse aspect ratio $a/R_0 = 0.358$, ion temperature profile $R_0/L_T = 6.92\exp\{-[(r-0.5)/0.28]^6\}$, $T_e/T_i = 1$, $q = 0.854 + 2.184r^2$, and $L_T/L_n = 0.319$.

The linear benchmark simulations are carried out in a radial domain from 0.2 to 0.8 (in terms of normalized minor radius), and the ITG instability is measured at $r = 0.5$ where the temperature gradient peaks. As illustrated in Fig.4, good agreement is obtained for the real frequencies ω_r, while the growth rates γ of the higher-n modes from the general geometry GTC are slightly lower. The overall difference in frequency magnitude $|\omega|$ is less than 5%. The contour plots of the electrostatic potential perturbation on a poloidal plane show quite similar eigenmode structures from the two simulations.

In the nonlinear ITG benchmark, the velocity space nonlinearity is included, which may have considerable effect on turbulence dynamics.[39] Flat marker temperature and density profiles are used in the general geometry GTC for the benchmarks only. The radial simulation domain here is from $r = 0.1$ to $r = 0.9$. As shown in Fig.5, the nonlinear benchmark results are in good agreement for both steady state heat flux and zonal flow over the entire radial domain. It is also found that the self-generated zonal flow in ITG turbulence has a spatial scale of the order of the turbulence radial extension, with a roughly odd parity.

It is well known that electrostatic turbulence with adiabatic electrons does not drive particle transport across the magnetic field lines. This result can be used as a rigorous test for a complex simulation such as that developed in this paper. In the Fig. 6 the heat flux, and the energy flux which is the sum of the heat flux and the convective energy flux carried by the particle flux, vs time at $r = 0.46$ are plotted. The result that the energy flux and heat flux are the same indicates that, indeed, no particle flux is produced in the simulation. Moreover, the particle flux is driven nowhere over the entire radial domain ($0.1 \leq r \leq 0.9$) of the global simulation.

B. Nonlocal ITG modes and global turbulence dynamics

Most previous linear analysis of microinstability has been carried out locally, neglecting the radial variation of equilibrium quantities such as pressure gradient and pressure itself. While GTC is a global toroidal code, in order to focus on the simplest problems involving shear effects due to the radial variation of the pressure gradient, the plasma temperature and density were assumed constant in the previous simulations. While such a treatment is well-motivated

and useful in separating and clarifying fundamental physics issues, it does not realistically capture the comprehensive global physics. In Fig. 7, we present an example of global ITG instability from the simulation of the general geometry model, taking into account the radial variation of temperature and density consistent with their gradient profiles. Compared to the simulation with constant T and n, the ITG growth rate is considerably reduced, with no significant change in the real frequency. Meanwhile, the contour plot of the electric potential on a poloidal plane shows that the eigenmode structure is twisted in the poloidal direction.

We have also applied our new nonlinear ITG simulation capability to a shaped toroidal plasma, based on the DIII-D experiment with the same model profiles as in Fig. 7. First, we examine the global turbulence evolution dynamics. The spatio-temporal evolution of the flux surface averaged turbulence intensity is plotted in Fig. 8. The turbulence is driven by the ion temperature gradient initially in the linearly unstable region ($0.42 < r < 0.76$), and then fluctuations spread in both the inward and outward radial directions into the linearly stable regions, leading to radially global turbulence and transport nonlocality. The fluctuation intensity level in the stable regions is comparable to that in the original unstable regions. Also presented are three snapshots of the electric potential contour plot on a poloidal plane, which illustrate the dynamic, global evolution of turbulence. At an early time before the nonlinear saturation, radially elongated streamers are generated in the linearly unstable region with small extension into the linearly stable zone via linear toroidal coupling.[40] Later on, turbulence eddies are broken up by the self-generated $\mathbf{E} \times \mathbf{B}$ shearing flows (zonal flows) during the nonlinear saturation phase. A fast radial expansion of the fluctuations, with associated nonlinear toroidal coupling, immediately follows as the streamers are broken into smaller radial scale (higher radial wave number) fluctuations by the zonal flows. At a later time, they evolve into widely spread global turbulence – this establishes the coupling between linearly stable and unstable regions.

C. Turbulence self-regulation in collisionless plasma

One of the key components in ITG turbulence is the zonal flow which regulates the turbulence level locally.[41] Figure 9 illustrates the mutual self-regulation between the zonal flow and the

turbulence. There exists a threshold for zonal flow excitation and a complex causal relation between the turbulence and the zonal flow. In this collisionless simulation, the observed oscillations in turbulence intensity and zonal flow energy can be generally attributed to the nonlinear interplay process in which the turbulence drives the zonal flow which, in turn, reduces the turbulence to a lower level. These oscillations should not be confused with the faster oscillations associated with the geodesic acoustic modes (GAM). It should be pointed out that the nonlinear oscillation shown here is different than that previously observed in Ref. 17, which is associated with the collisional damping of zonal flow.[42]

When the zonal flows are artificially excluded, our simulation shows that turbulence intensity does not oscillate after saturation. This clearly indicates that the oscillation behavior results from nonlinear interplay between turbulence and zonal flows. Note that similar properties for the zonal flow and drift wave system have been demonstrated in simple analytical models[43,44] in which, however, only the collisional damping of zonal flow is explicitly assumed. Here, the nonlinear oscillations shown in Fig. 9 occur with collisionless zonal flows. The apparent nonlinear collisionless damping processes, which are responsible for the saturation of zonal flows and the nonlinear oscillations shown in Fig. 9, are not theoretically understood yet. The candidates may include the "tertiary instability",[45] generalized Kelvin-Helmholtz (GKH) instability,[46] and the energy transfer to parallel sound waves and turbulence via poloidally asymmetric pressure perturbations,[47] etc.

Next, we attempt to clarify the possibility of energy transfer from zonal flow back to turbulence. In a consistent simulation, it is hard to identify this process from the entire nonlinear evolution of the system. Here we perform a carefully designed numerical experiment to examine this process. The simulation uses the same parameters as in Fig. 8. We introduce artificial zonal flows in the regions where the ITG mode is linearly (and also nonlinearly) stable ($r < 0.42$ and $r > 0.76$). The artificial zonal flows are driven via adding in Eq. (18) a nonzero axisysmmetric density fluctuation $\langle \delta \bar{n}_i \rangle / n_0$ which is a certain (small) friction of that in the unstable region ($0.42 < r < 0.76$). The spatio-temporal evolution of the turbulence intensity is plotted in Fig. 10(a). Comparing to the previous simulation of Fig. 8, this shows that, in the presence of artificial zonal flows, potential fluctuations are driven to grow in the regions where the ITG is stable. This fluctuation growth in the early phase occurs before

the propagation front of ITG turbulence from the unstable region reaches the stable region. The temporal evolution of zonal flow energy and turbulence intensity at $r = 0.33$ (ITG stable region) plotted in Fig. 10(b) shows two interesting properties: i) the turbulence components are temporally delayed relative to the zonal flow which is artificially excited at the same time as that in the unstable ITG region; ii) there is an amplitude threshold for zonal flow to excite turbulence. Both are clear indications of a relation, that zonal flows can drive turbulence. This can be compared with the zonal flow generation process in the ITG-unstable region: Fig. 10(c) shows that zonal flows are excited after the ITG driven turbulence grows to a certain level. As mentioned before, this simulation uses artificially driven zonal flows to demonstrate the possibility that zonal flows can drive turbulence, which would be difficult to identify in a self-consistent simulation with complex nonlinear dynamics. It is also interesting to examine the zonal flow generation process in the ITG stable region in the consistent simulation of Fig. 8. The result here is presented in Fig. 10(d), which shows that zonal flows are excited by turbulence which has spread in.

After establishing the fact that zonal flows can drive turbulence, the next question is, how efficiently can the energy be transfered from the zonal flows to the turbulence. Figure 11 shows the temporal evolution of zonal flow energy $< |\nabla \phi_{00}|^2 >$, and turbulence energy $< |\nabla \delta\phi|^2 >$. It is found that the saturated turbulence energy is two orders of magnitude smaller than that of the zonal flows. Note that, in Fig. 11, the second growth in turbulence energy, starting at $t \sim 270$, is caused by the spreading of the ITG driven turbulence originating in the region $0.42 < r < 0.76$. Our numerical experiments also show that the above observations are not sensitive to the strength and the profile shape of the artificially excited zonal flows. In contrast, the zonal flow generation by the turbulence in the ITG unstable region is very efficient in the sense that, during their generation process, zonal flows extract a large amount of energy from the turbulence components. Therefore, our simulation results suggest that zonal flows can drive turbulence. However, this process is too weak to be an effective zonal flow saturation mechanism.

IV. SUMMARY

We have presented a generalized model which incorporates important realism of tokamak experiments into nonlinear gyrokinetic simulations of plasma turbulence. These include a systematic treatment of plasma rotation and equilibrium $\mathbf{E} \times \mathbf{B}$ flow, realistic plasma profiles and corresponding magnetohydrodynamic (MHD) equilibria. The general geometry simulation capability has been developed with following favorable features: i) By rescaling the radial coordinate, the grid size in the perpendicular direction is correlated with the local gyroradius which, varying substantially from the core to the edge, defines the spatial scale of turbulence at different locations. ii) Gyrokinetic transformations of potential and charge density between particle and guiding center positions are calculated with a finite ratio (B_θ/B) correction which is a significant geometry effect on the turbulence calculation, particularly for spherical torus devices. iii) The applied equilibrium $\mathbf{E} \times \mathbf{B}$ flow with the spatial scale of the plasma minor radius, which is believed to play an important role in determining the turbulence level, is calculated from our first-principles based particle simulation of global neoclassical dynamics with important finite orbit effects. Working with a symmetry coordinate system, we can construct a relatively regular mesh in real space for strongly shaped toroidal plasmas. This also facilitates straightforward visualization. In the large aspect ratio circular concentric geometry limit, cross benchmarks of the linear and nonlinear characteristics, such as real frequency, growth rate, steady-state heat flux and zonal flow amplitude, of ITG turbulence have been carried out to validate the general geometry model and simulation.

Our nonlinear simulations have been applied to a DIII-D shaped plasma to examine both local and nonlocal phenomena of ITG turbulence. The dynamic evolution from the radially elongated streamers generated by localized instability, to short radial scale fluctuations due to the shearing decorrelation of the zonal flows, and then to radially global turbulence via turbulence spreading into linearly unstable regions, has been demonstrated. The coupling established between linearly stable and unstable regions via turbulence spreading, as shown in our simulation, may explain some experimental reports of the existence of finite density fluctuations and anomalous heat transport in the linearly stable region inside an internal transport barrier.[48] With regard to the nonlinear interplay between zonal flow and turbu-

lence, our numerical experiments suggest that the zonal flows can drive turbulence. However, the associated energy coupling is too weak to provide sufficient zonal flow damping to be responsible for zonal flow saturation and the bursting behavior in the fluctuations observed in our collisionless simulations.

ACKNOWLEDGMENTS

One of authors (Wang) would like to acknowledge Drs. R. White and L. Zakharov for help with the MHD equilibrium interface and useful discussions, and Drs. A. Boozer, L. Chen, P. Diamond, R. Goldston, F. Hinton, R. Nazikian, and X. Tang for valuable discussions.

This work was supported by the U.S. Department of Energy (DoE) Scientific Discovery through Advanced Computing (SciDAC) Center for Gyrokinetic Particle Simulation, and by DoE Contract No DE-AC02-CHO-3073.

[1] W. M. Tang, Nucl. Fusion **18**, 1089 (1978).

[2] J. W. Connor and H. R. Wilson, Plasma Phys. Control. Fusion **36**, 719 (1994).

[3] W. Horton, Rev. Mod. Phys. **71**, 735 (1999).

[4] S. Parker, W. Lee, and R. Santoro, Phys. Rev. Lett. **71**, 2042 (1993).

[5] M. Kotschenreuther, G. Rewoldt, and W. M. Tang, Comput. Phys. Commun. **88**, 128 (1995).

[6] R. D. Sydora, V. K. Decyk, and J. M. Dawson, Plasma Phys. Control. Fusion **38**, A281 (1996).

[7] M. A. Beer and G. W. Hammett, Phys. Plasmas **3**, 4046 (1996).

[8] Z. Lin, T. S. Hahm, W. W. Lee, W. M. Tang and R. White, Science **281**, 1835 (1998).

[9] W. Dorland, *Proc. 18th Intnl. Conf. on Fusion Energy, Sorrento, Italy, 2000*, (International Atomic Energy Agency).

[10] A. M. Dimits et al., Phys. Plasmas **7**, 969 (2000).

[11] F. Jenko, Comput. Phys. Commun. **125**, 196 (2000).

[12] J. Candy and R. Waltz, J. Comput. Phys. **186**, 545 (2003).

[13] Y. Chen and S. Parker, J. Comput. Phys. **189**, 463 (2003).

[14] Y. Idomura, S. Tokuda and Y. Kishimoto, Nucl. Fusion **43**, 243 (2003).

[15] L. Villard et al., Nucl. Fusion **44**, 172 (2004).

[16] W. W. Lee, Phys. Fluids **26**, 556 (1983).

[17] Z. Lin, T. S. Hahm, W. W. Lee, W. M. Tang, and P. H. Diamond, Phys. Rev. Lett. **83**, 3645 (1999).

[18] Z. Lin, S. Ethier, T. S. Hahm, and W. M. Tang, Phys. Rev. Lett. **88**, 1950004 (2002).

[19] Z. Lin and T. S. Hahm, Phys. Plasmas **11**, 1099 (2004).

[20] T. S. Hahm, P. H. Diamond, Z. Lin, K. Itoh, and S.-I. Itoh, Plasma Phys. Control. Fusion **46**, 323 (2004).

[21] T. S. Hahm, P. H. Diamond, Z. Lin, G. Rewoldt, O. Gurcan, and S. Ethier, Phys. Plasmas **12**, 090903 (2005).

[22] R. White and L. E. Zakharov, Phys. Plasmas **10**, 573 (2003).

[23] R. J. Littlejohn, Phys. Fluids **24**, 1730 (1981).

[24] E. A. Frieman and L. Chen, Phys. Fluids **25**, 502 (1982).

[25] D. H. E. Dubin, J. A. Krommes, C. Oberman, and W. W. Lee, Phys. Fluids **26**, 3524 (1983).

[26] T. S. Hahm, Phys. Fluids **31**, 2670 (1988).

[27] A. J. Brizard, J. Plasma Phys. **41**, 541 (1989).

[28] T. S. Hahm, Phys. Plasmas **3**, 4658 (1996).

[29] W. W. Lee, J. Comput. Phys. **72**, 243 (1987).

[30] Z. Lin and W. W. Lee, Phys. Rev. E **52**, 5646 (1995).

[31] F. L. Hinton and S. K. Wong, Phys. Fluids **28**, 3028 (1985).

[32] W. X. Wang, F. L. Hinton, and K. Wang, Phys. Rev. Lett. **87**, 055002 (2002).

[33] W. X. Wang, W. M. Tang, F. L. Hinton, L. E. Zakharov, R. B. White, and J. Manickam, Comput. Phys. Commun. **164**, 178 (2004).

[34] Z. Lin and L. Chen, Phys. Plasmas **8**, 1447 (2001).

[35] W. X. Wang, L. Chen, and Z. Lin, Bull. Am. Phys. Soc. **46**(7), 114 (2001).

[36] I. Manuilskiy and W. W. Lee, Phys. Plasmas **7** 1381 (2000).

[37] J. L. V. Lewandowski, Phys. Plasmas **10**, 3204 (2003).

[38] Y. Nishimura, Z. Lin, J. L. V. Lewandowski, and S. Ethier, J. Comput. Phys. (to be published).

[39] W. W. Lee, Bull. Am. Phys. Soc. **49**(8), 135 (2004).

[40] X. Garbet, L. Laurent, A. Samain, and J. Chinardet, Nucl. Fusion **34**, 963 (1994).

[41] P. H. Diamond, K. Itoh, S.-I. Itoh, and T. S. Hahm, Plasma Phys. Control. Fusion **47**, R35 (2005).

[42] F. L. Hinton and M. N. Rosenbluth, Plasma Phys. Control. Fusion **41**, A653 (1999).

[43] M. A. Malkov, P. H. Diamond, and M. N. Rosenbluth, Phys. Plasmas **8**, 5073 (2001).

[44] R. White, L. Chen, and F. Zonca, Phys. Plasmas **12**, 057304 (2005).

[45] B. N. Rogers, W. Dorland, and M. Kotschenreuther, Phys. Rev. Lett. **85**, 5336 (2000).

[46] E. J. Kim and P. H. Diamond, Phys. Plasmas **9**, 4530 (2002).

[47] N. Miyato, Y. Kishimoto, and J. Li, Phys. Plasmas **12**, 5557 (2004).

[48] R. Nazikian et al., Phys. Rev. Lett. **94**, 135002 (2005).

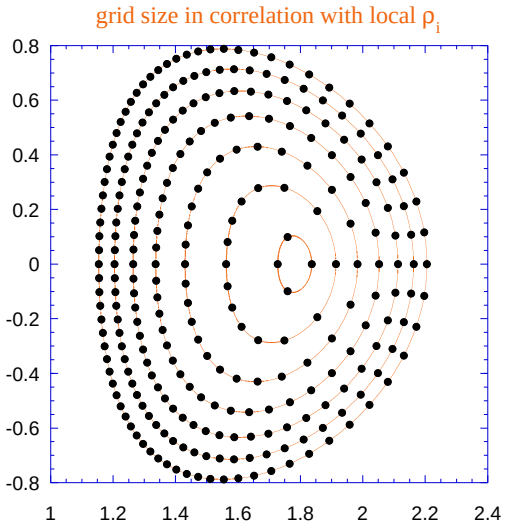

Figure 1: An example of a nonuniform grid on a poloidal plane showing grid size in correlation with local ion gyroradius.

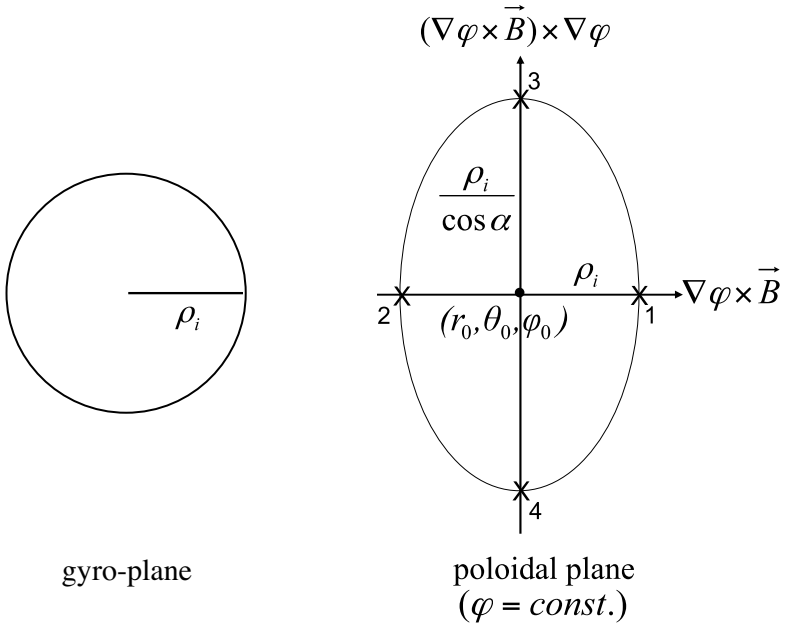

Figure 2: Ion gyro-orbit.

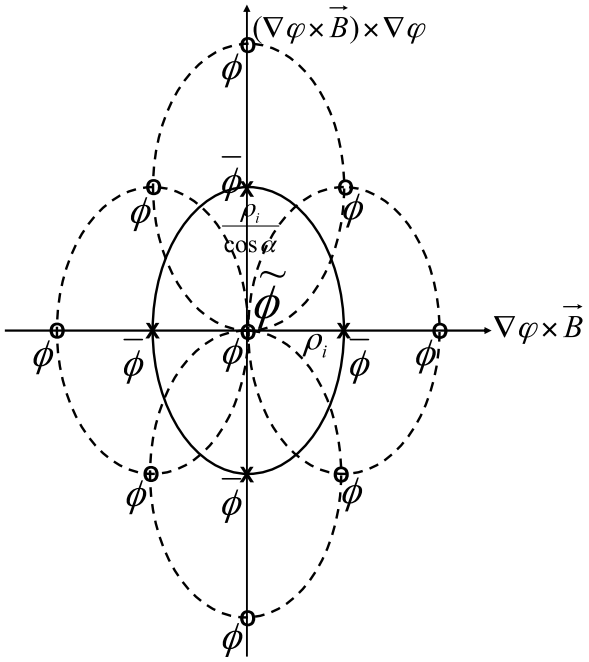

Figure 3: Schematic diagram of double average process for calculating $\tilde{\phi}$ at the center position.

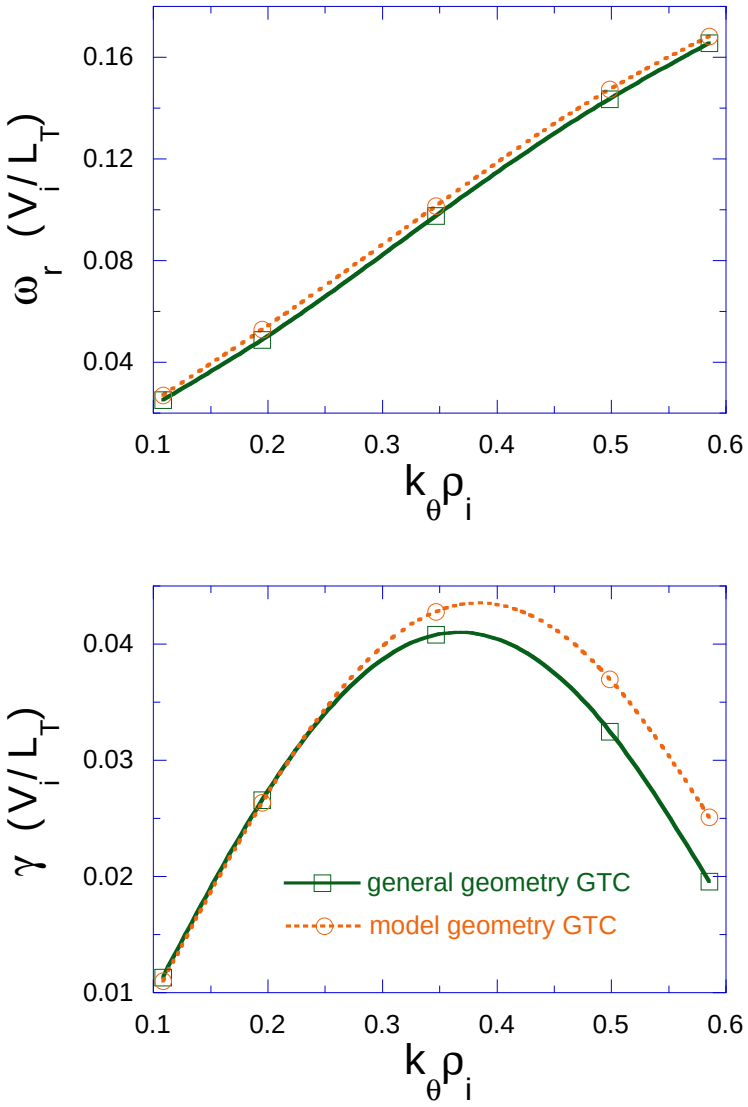

Figure 4: Real frequency ω_r and growth rate γ of ITG instability versus poloidal wave number k_θ, compared with the original GTC calculation.

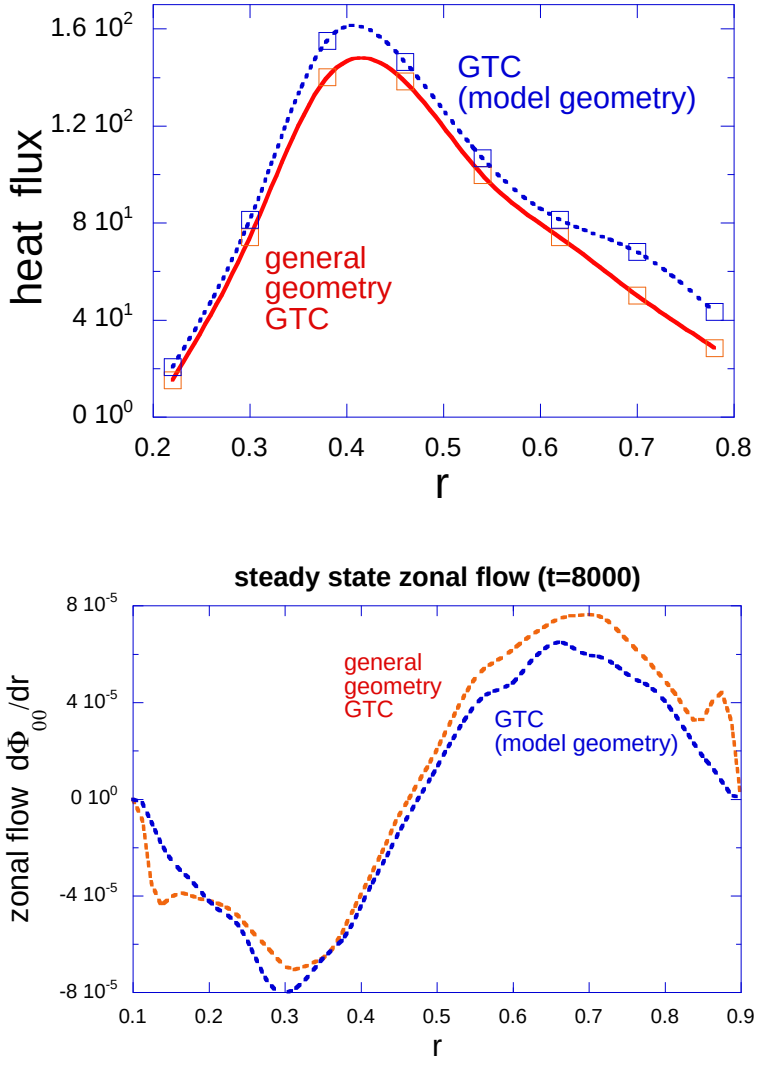

Figure 5: Steady state heat flux profile and zonal flow profile of nonlinear ITG simulation with simple magnetic geometry, compared with the original GTC result.

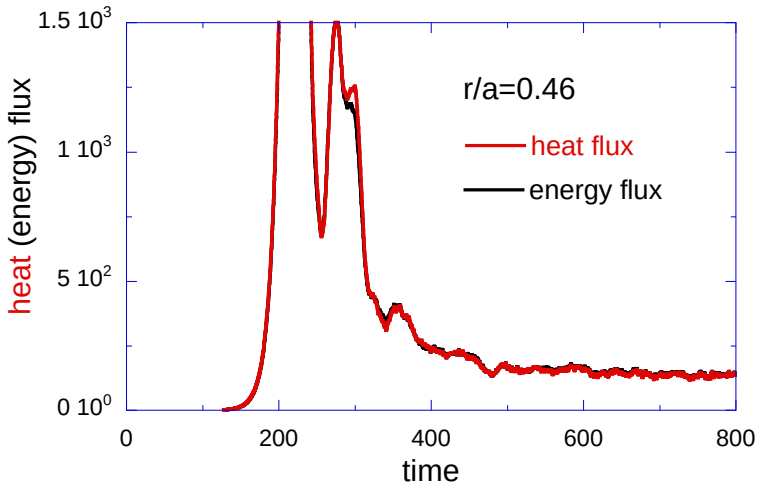

Figure 6: Temporal history of ion heat and energy flux of ITG turbulence with adiabatic electrons (from the simulation of the general geometry model).

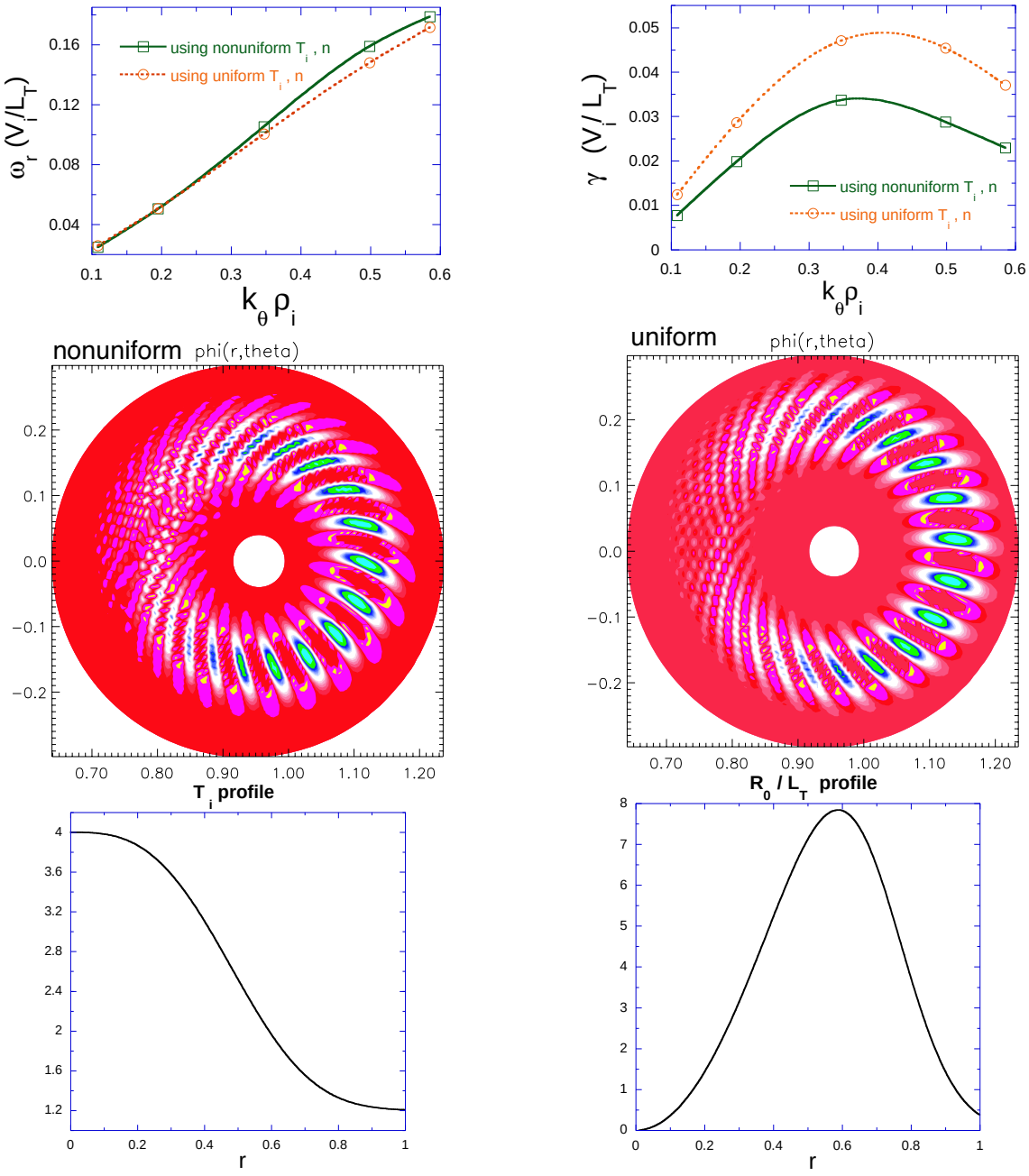

Figure 7: Simulation results of a nonlocal ITG instability using radially varying temperature and density, compared with the simulation neglecting the effects of radial shear of temperature and density: real frequency ω_r (upper-left) and growth rate γ (upper-right) vs $k_\theta \rho_i$; contour plot of electric potential from simulation with nonuniform T and n (middle-left) and simulation without the effects of T and n shear (middle-right); ion temperature profile (lower-left) and corresponding gradient profile(lower-right) used in the simulations.

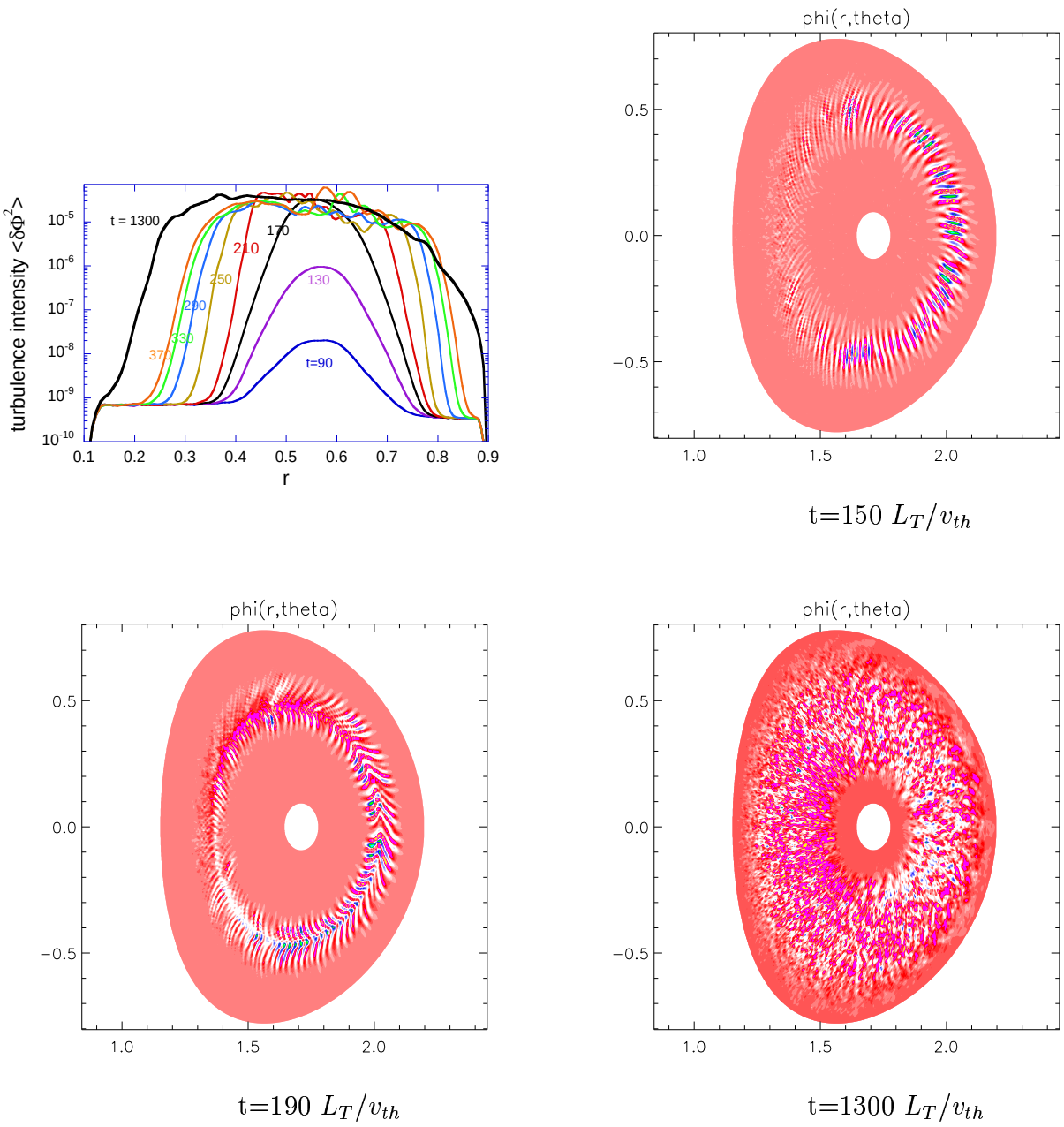

Figure 8: Spatio-temporal evolution of flux surface averaged turbulence intensity (upper), and three snapshots of contour plot of electric potential on a poloidal plane (lower) from a simulation of a shaped plasma with typical DIII-D parameters.

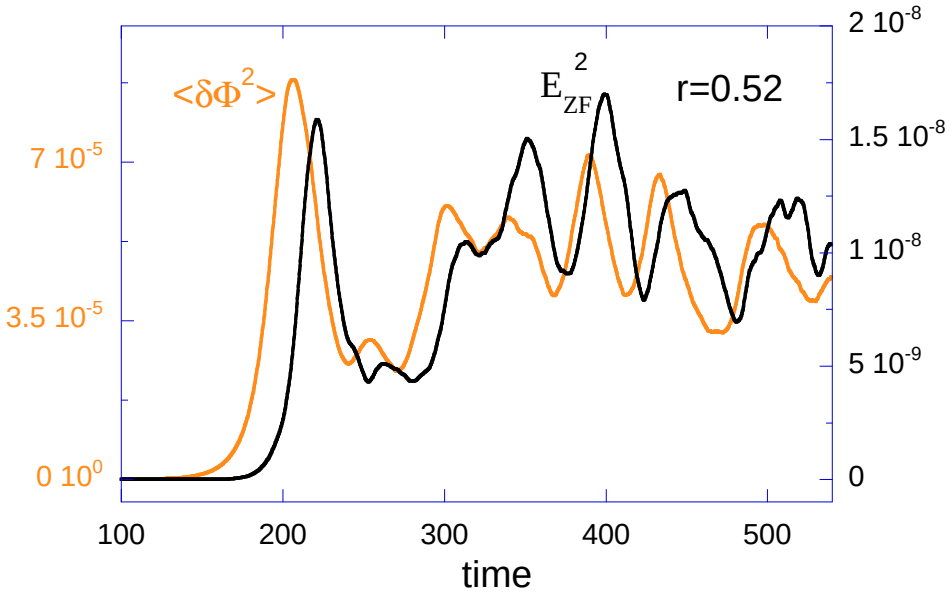

Figure 9: Temporal evolution of turbulence intensity $< \delta\Phi^2 >$ and zonal flow energy $E_{ZF}^2 \propto |d\phi_{00}/dr|^2$ at $r = 0.52$ (from the same simulation as Fig. 8).

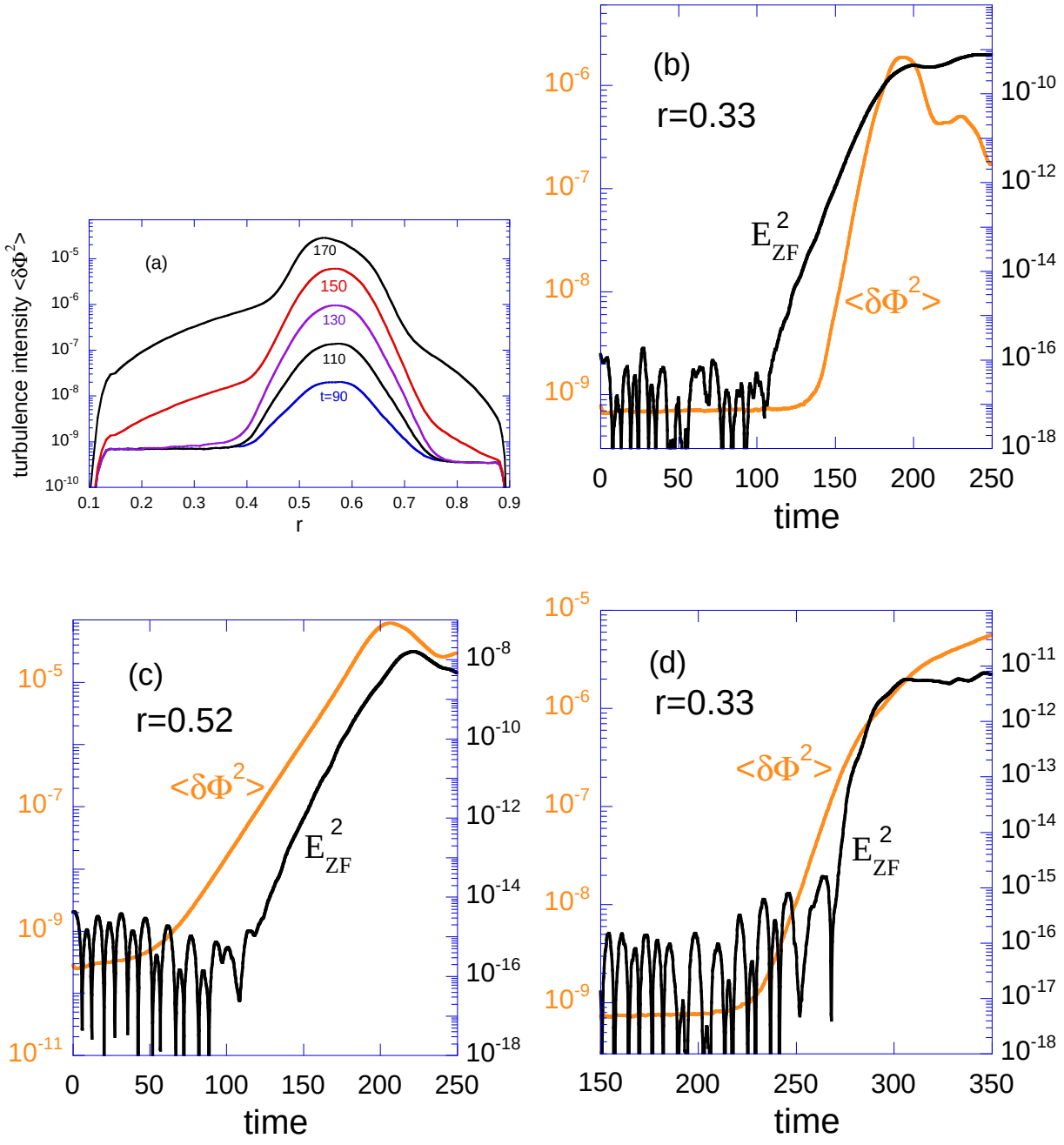

Figure 10: (a) Spatio-temporal evolution of turbulence intensity $< \delta\Phi^2 >$ from a simulation with artificial zonal flows introduced in the ITG stable regions $r < 0.42$ and $r > 0.76$; (b) temporal evolution of zonal flow energy $E_{ZF}^2 \propto |d\phi_{00}/dr|^2$ and turbulence intensity at an ITG stable location $r = 0.33$; temporal evolution of zonal flow energy and turbulence intensity at (c) $r = 0.52$ (linearly unstable region) and (d) $r = 0.33$ (linearly stable region) from the self-consistent simulation of Fig. 8.

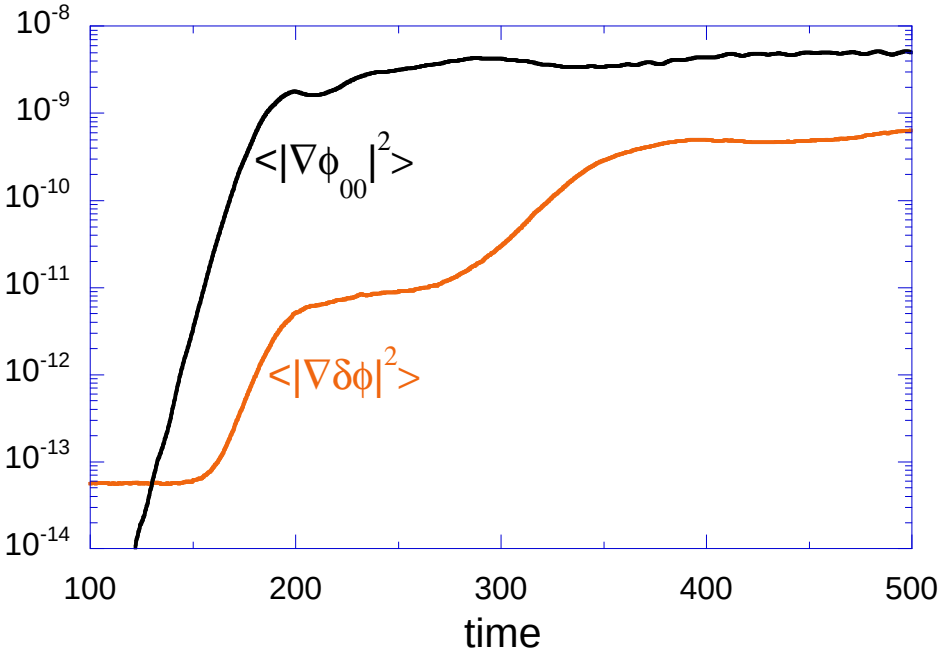

Figure 11: Temporal evolution of energy contained in artificial zonal flows and in driven turbulence at an ITG stable location $r = 0.33$.

External Distribution

Plasma Research Laboratory, Australian National University, Australia
Professor I.R. Jones, Flinders University, Australia
Professor João Canalle, Instituto de Fisica DEQ/IF - UERJ, Brazil
Mr. Gerson O. Ludwig, Instituto Nacional de Pesquisas, Brazil
Dr. P.H. Sakanaka, Instituto Fisica, Brazil
The Librarian, Culham Science Center, England
Mrs. S.A. Hutchinson, JET Library, England
Professor M.N. Bussac, Ecole Polytechnique, France
Librarian, Max-Planck-Institut für Plasmaphysik, Germany
Jolan Moldvai, Reports Library, Hungarian Academy of Sciences, Central Research Institute for Physics, Hungary
Dr. P. Kaw, Institute for Plasma Research, India
Ms. P.J. Pathak, Librarian, Institute for Plasma Research, India
Dr. Pandji Triadyaksa, Fakultas MIPA Universitas Diponegoro, Indonesia
Professor Sami Cuperman, Plasma Physics Group, Tel Aviv University, Israel
Ms. Clelia De Palo, Associazione EURATOM-ENEA, Italy
Dr. G. Grosso, Instituto di Fisica del Plasma, Italy
Librarian, Naka Fusion Research Establishment, JAERI, Japan
Library, Laboratory for Complex Energy Processes, Institute for Advanced Study, Kyoto University, Japan
Research Information Center, National Institute for Fusion Science, Japan
Professor Toshitaka Idehara, Director, Research Center for Development of Far-Infrared Region, Fukui University, Japan
Dr. O. Mitarai, Kyushu Tokai University, Japan
Mr. Adefila Olumide, Ilorin, Kwara State, Nigeria
Dr. Jiangang Li, Institute of Plasma Physics, Chinese Academy of Sciences, People's Republic of China
Professor Yuping Huo, School of Physical Science and Technology, People's Republic of China
Library, Academia Sinica, Institute of Plasma Physics, People's Republic of China
Librarian, Institute of Physics, Chinese Academy of Sciences, People's Republic of China
Dr. S. Mirnov, TRINITI, Troitsk, Russian Federation, Russia
Dr. V.S. Strelkov, Kurchatov Institute, Russian Federation, Russia
Kazi Firoz, UPJS, Kosice, Slovakia
Professor Peter Lukac, Katedra Fyziky Plazmy MFF UK, Mlynska dolina F-2, Komenskeho Univerzita, SK-842 15 Bratislava, Slovakia
Dr. G.S. Lee, Korea Basic Science Institute, South Korea
Dr. Rasulkhozha S. Sharafiddinov, Theoretical Physics Division, Insitute of Nuclear Physics, Uzbekistan
Institute for Plasma Research, University of Maryland, USA
Librarian, Fusion Energy Division, Oak Ridge National Laboratory, USA
Librarian, Institute of Fusion Studies, University of Texas, USA
Librarian, Magnetic Fusion Program, Lawrence Livermore National Laboratory, USA
Library, General Atomics, USA
Plasma Physics Group, Fusion Energy Research Program, University of California at San Diego, USA
Plasma Physics Library, Columbia University, USA
Alkesh Punjabi, Center for Fusion Research and Training, Hampton University, USA
Dr. W.M. Stacey, Fusion Research Center, Georgia Institute of Technology, USA
Director, Research Division, OFES, Washington, D.C. 20585-1290

The Princeton Plasma Physics Laboratory is operated
by Princeton University under contract
with the U.S. Department of Energy.

Information Services
Princeton Plasma Physics Laboratory
P.O. Box 451
Princeton, NJ 08543

Phone: 609-243-2750
Fax: 609-243-2751
e-mail: pppl_info@pppl.gov
Internet Address: http://www.pppl.gov